4.4.2
Protective Coatings for Gas Turbines

Kang N Lee

Cleveland State University
NASA Glenn Research Center
Cleveland, OH 44135

Current Address:
Rolls-Royce Corpation
P.O. Box 420, Speed Code W-08
Indianapolis, IN 46206

phone: 317-230-4469
email: kang.n.lee@rolls-royce.com

4.4.2-1 Introduction

Economical and environmental concerns, i.e. improving efficiency and reducing emissions, are the main driving force behind the ever increasing demand for higher gas turbine engine inlet temperatures. Technology improvements in cooling, materials and coatings are required to achieve higher inlet temperatures[1]. Advances in the development of airfoil cooling designs have been achieved by combining high convective cooling efficiencies with film cooling.

Material improvements have been dramatic during the past several decades. The improvement in alloy composition and the development of directional and single crystal casting technologies have allowed increased alloy operation temperatures, and hence increased turbine inlet temperatures[2]. Improved high temperature mechanical properties of alloys, however, have been made typically at the expense of environmental resistance. This trend, combined with higher operating temperatures, has resulted in environmental degradation of materials, deteriorating the mechanical properties and shortening the service life of components[3]. The need to protect alloys from environmental degradation motivated the development of protective coatings. The idea to apply a layer with protective properties on the surface of Ni-based superalloys was first practiced in the 1960s[4]. Two types of protective coatings have been most widely used: diffusion aluminide coatings based on β-NiAl phase and MCrAlY (M = Ni, Co, or NiCo) overlay coatings based on a mixture of β-NiAl and γ'-Ni_3Al or γ phases[5].

As the temperature capability of Ni-based superalloys approaches their intrinsic limit, further improvements in their temperature capability have become increasingly difficult[6]. Therefore, during the past two decades, the emphasis in gas turbine materials developments has shifted to thermal barrier coatings (TBC), which are ceramic coatings with a very low thermal conductivity that reduce the alloy surface temperature by insulating it from the hot gas. Current state-of-the-art thermal barrier coatings comprise two layers: a diffusion aluminide or MCrAlY bond coat and a low thermal conductivity partially stabilized zirconia (YSZ: 7 to 8 wt% Y_2O_3-ZrO_2) top coat. Thermal barrier coatings were first successfully tested in a research turbine engine in mid 70s. By the early 80s they entered revenue service on the vane platforms of aircraft engines, and today they are flying in revenue service on vane and blade surfaces[7]. Thermal barrier coatings are expected to play an increasingly significant role in advanced gas turbine engines both in aero and industrial applications in the future.

Major improvements in turbine inlet temperatures can be achieved by replacing Ni-based superalloy hot section components with silicon-based ceramic matrix composite (CMC) and silicon nitride (Si_3N_4) ceramics[8]. These materials have superior high temperature mechanical properties, such as strength and creep resistance, compared to Ni-based superalloys. They are also light and possess excellent high temperature oxidation resistance in clean, dry air, due to the formation of slow-growing, protective silica scale[9]. One major disadvantage of these materials is the lack of environmental durability in combustion environments. Water vapor, a combustion reaction product, reacts with the protective silica scale, forming gaseous reaction products, such as $Si(OH)_4$ [10]. In high pressure, high gas velocity combustion environments, this reaction results in rapid recession of these materials. These materials also suffer from severe hot corrosion in environments contaminated by molten salt[11].

A new class of coatings, environmental barrier coating (EBC), has been developed in the 90s to protect Si-based ceramics and ceramic composites from the degradation by water vapor[12]. The current state-of-the-art environmental barrier coating comprises three layers: a silicon bond coat, a mullite-based intermediate coat, and a barium-strontium-aluminosilicate ($1\text{-}xBaO{\cdot}xSrO{\cdot}Al_2O_3{\cdot}2SiO_2$, $0 \le x \le 1$) top coat[13]. CMC combustor liners coated with the current state of the art EBC were retrofitted in a Solar Turbines' industrial gas turbine engine and successfully completed a 14,000 h field test in the late 90s[14].

This paper will discuss the status of current thermal barrier coatings and environmental barrier coatings, with the focus on key factors affecting their performance.

4.4.2-2a Coatings for Superalloy Components

Current thermal barrier coatings consist of two layers: a metallic bond coat and a ceramic top coat[15]. The bond coat has two key functions: It provides the bonding between the ceramic top coat and the superalloy substrate and protects the superalloy from the environmental degradation. The key function of the ceramic top coat is to reduce the alloy surface temperature by insulating it from the hot gas.

Current bond coats are diffusion aluminide coatings based on β-NiAl phase and MCrAlY (M = Ni, Co, or NiCo) coatings based on a mixture of β-NiAl and γ'-Ni_3Al or γ phases[16]. Bond coats oxidize upon thermal exposure, even in the presence of a ceramic top coat, forming an oxide scale, known as TGO (thermally grown oxide). Current top coat is yttria-stabilized zirconia (YSZ: ZrO_2 doped with 7~8 wt% Y_2O_3). YSZ has several important characteristics for a successful top coat[17]. It has a high melting point, a low thermal conductivity and a high thermal expansion coefficient and is thermodynamically stable in contact with alumina that grows on bond coat. The ZrO_2-7~8 wt% Y_2O_3 composition also has good erosion resistance compared with other ceramics and good phase stability at temperatures <1200°C.

The durability of thermal barrier coatings is governed by a sequence of crack nucleation, propagation and coalescence events along the bond coat/TGO or top coat/TGO interfaces that accumulate prior to final failure by large scale buckling or edge lifting[18]. Stresses in TBC play an important role in crack nucleation. TBC stresses arise from two sources: stresses due to TGO growth and stresses due to the coefficient of thermal expansion (CTE) mismatch between the various layers. Therefore, the bond coat must form the most protective oxide scale possible which, in practice, means an alumina scale that is slow-growing, and adherent[19]. The nature of stresses in TBC is closely related to the surface roughness of bond coat. Both growth and CTE mismatch stresses are compressive on flat bond coat surfaces[20]. The thermal mismatch stress (σ_t) is given by,

$$\sigma_t = (\alpha_c - \alpha_{substrate})\,\Delta T\, E_c/(1-\nu_c) \quad (1)$$

where α_c and $\alpha_{substrate}$ are coefficients of thermal expansion for the coating and the substrate, respectively, E_c is the Young's modulus of the coating, and ν_c is the Possion's ratio of the coating. Therefore, YSZ having a lower CTE than the bond coat and superalloy substrate is expected to be in compression on cooling, assuming stresses are relaxed at high temperatures. However, the surface of an initially flat bond coat gradually roughens with thermal exposures, forming TGO with a convoluted morphology and major imperfections[21]. Rough bond coat surfaces produce out-of-plane stresses along the bond coat/TGO or top coat/TGO interfaces[22]. These local out-of-plane stresses are responsible for the nucleation of cracks which ultimately lead to the failure of TBC.

There are two degradation mechanisms for YSZ that have significant effects on TBC stresses: Phase transformation[23] and sintering of YSZ[24]. These changes result in higher thermal stresses and a decrease in thermal fatigue life. Sintering also causes an increase in thermal conductivity. Two approaches have been investigated to alleviate the high-temperature durability problems of YSZ[25]: the first approach is alternative stabilizers for ZrO_2 and the second approach is alternative materials to ZrO_2.

Key factors affecting TBC performance to be discussed in subsequent sections are bond coat surface finish, bond coat oxidation, bond coat surface imperfections, thermal conductivity of YSZ, sintering of YSZ, and phase transformation of YSZ.

4.4.2-2b Bond Coat

Processing

Pack cementation and chemical vapor deposition are widely used methods to form diffusion aluminide coatings on turbine blades. Pack cementation is a chemical vapor deposition process in which component surface is saturated with aluminum in a powder mixture containing aluminum, aluminum oxide (as an inert filler) and a halide activator (usually NH_4Cl)[26]. When the reactor containing the components to be coated and the powder mixture is heated, aluminum halides ($AlCl_3$, $AlCl_2$, AlCl) form which diffuse through the powder mixture and react with the components, resulting in the formation of an aluminide coating. In practice, platinum is added in β-NiAl bond coat to form platinum modified diffusion aluminide coating, (Ni,Pt)Al, which significantly improves the alumina scale adherence[27]. In this process, components are electroplated with a thin Pt layer prior to the aluminization.

The aluminizing process can be divided into a high, medium, and low activity process[28]. The main phases of the outer zone of the coatings in high, medium, and low activity process are $NiAl_3$+Ni_2Al_3 (>40 wt.% Al), NiAl (32-38 wt.% Al) and NiAl or NiAl+Ni_3Al (<31 wt.% Al), respectively[29]. Lower activity process produces coatings with higher ductility. A typical as-aluminized (Ni,Pt)Al bond coat surface exhibits large grains of Pt-modified β-NiAl with a cellular network of grain-boundary ridges, whose geometry is very similar to that of underlying bond coat grain boundary structure[30].

Low Pressure Plasma Spaying (LPPS) and Electron Beam Physical Vapor Deposition (EB-PVD) are widely used methods to deposit overlay MCrAlY bond coat on turbine components[31]. NiCrAlY bond coat consists of the following main phases: γ-Ni-based solid solution, γ'-Ni_3Al phase, β-NiAl phase, and α-Cr-based solid solution[32]. Alloying NiCrAlY with Co reduces the thermal stability of γ'-phase, decreases its quantity, and converts NiCoCrAlY into β+γ[33]. It is this phase condition that makes NiCoCrAlY bond coat highly ductile. For Example, EB-PVD-processed Ni-20Co-20Cr-8Al-0.5Y (wt%) has Al-rich β phase and Ni-solid solution γ phase[34].

Surface Finish

Bond coat surface finish depends on the type of process employed for ceramic top coat. Air plasma sprayed (APS) YSZ top coat employs a MCrAlY bond coat processed typically by low pressure plasma spraying (LPPS). Rough surface of as-processed MCrAlY bond coat facilitates good mechanical bonding to plasma-sprayed YSZ by providing anchoring points. EB-PVD YSZ top coat employs either a diffusion aluminide or a MCrAlY bond coat. In contrast to APS YSZ, the bond coat surface is treated to make it flat prior to the deposition of EB-PVD YSZ. This is to eliminate as-processed surface roughness which generates out-of-plane stresses. It may be that EB-PVD YSZ due to the nature of the process, i.e. vapor phase deposition in high temperature and vacuum, possesses good chemical bonding, eliminating the need for a rough surface for mechanical bonding. Typical surface treatment includes grit blasting, grinding, and shot peening.

Beneficial effects of grit blasting the bond coat surface with Al_2O_3 on TBC performance are discussed in Haynes, et al.[35]. The intensity of θ-Al_2O_3 was much lower on grit-blasted specimens compared to the as-processed bond coat surfaces. Grit blasting also eliminated the detrimental process of interfacial void growth during EB-PVD processing. It was suggested that grit blasting either suppressed θ-Al_2O_3 nucleation or triggered more rapid transformation to or nucleation of α-Al_2O_3 during EB-PVD process at ~1000°C. The elimination of void growth in the grit-blasted specimens was attributed to the removal of sulfur-contaminated zone at the surface of the bond coat. Lightly polishing the surface of as-deposited (Ni,Pt)Al bond coats prior to YSZ deposition also dramatically increased EB-PVD TBC life[36], presumably by the same mechanism by which grit blasting improved the TBC life.

Oxidation

The approach to achieving an 'ideal' α-alumina scale includes the addition of reactive element (RE), such as Y, Zr or Hf, the addition of precious metals such as Pt, and the desulfurization of the coating and superalloy substrate[37].

The addition of Pt to β-NiAl is known to improve alumina scale adhesion[38]. The Pt addition has the additional benefit of reducing the critical Al concentration necessary to form a protective α-Al_2O_3 scale in β-NiAl, suggesting that Pt improves selective oxidation to from alumina[39]. The addition of a reactive element, such as Zr, Hf, or Zr+Hf, to β-NiAl is more effective in improving the scale adhesion than the addition of Pt, and has the additional benefit of reducing the growth rate of α-Al_2O_3 scale[40]. Figure 1 shows that, at 1200°C, the addition of Hf reduces the scale growth rate by a factor of 40. Comparison of YSZ-coated Y-doped Rene N5 having a (Ni,Pt)Al bond coat and YSZ-coated β-NiAl+Zr showed that the change to a more oxidation-resistant bond coat composition increased the TBC lifetime by more than a factor of five at both 1150 and 1200°C[41]. The improvement was attributed to the formation of an adherent TGO on β-NiAl+Zr which was superior to that formed on (Ni,Pt)Al-coated Rene N5.

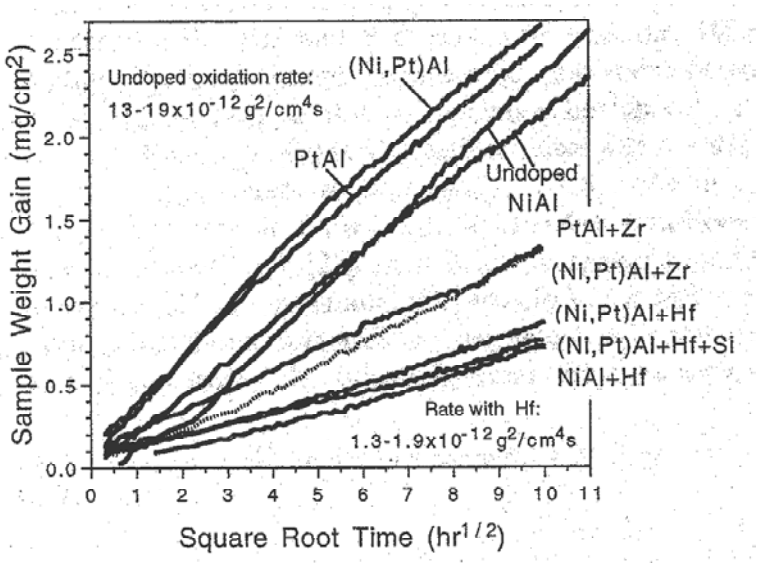

Fig. 1. Isothermal weight gains at 1200°C plotted versus the square root of time to show the parabolic reaction kinetics (Reprinted with permission of Elsevian, Copyright 1998)

Source: See Note 19. (Pint, et al.)

Sulfur is known to segregate to metal/scale interface, causing the deterioration of the scale adhesion by forming voids at the metal/scale interface[42]. Interfacial voids degrade the scale adhesion by limiting the contact between the metal and the scale and also by acting as a stress concentrator or crack initiator[43]. Consequently, lowering the level of S below ~1 ppm significantly improves the scale adhesion[44]. The beneficial effect of reactive elements (RE) in improving the scale adhesion has been attributed to the segregation of RE at the metal/scale interface which inhibits the interfacial segregation of sulfur impurity[45]. They also segregate to the oxide grain boundaries where they significantly reduce the outward transport of Al, thereby reducing the rate of oxide growth which is now mostly by oxygen transport[46]. The change in predominant growth mechanism also drastically reduces interfacial void formation since the flux of cation vacancies is reduced[47]. In practice, Hf is most effective in improving the oxidation resistance of β-NiAl and yet it does not have the same strong effect in superalloys or MCrAlY, in which Y is more effective[48]. Pt appears to improve the resistance to scale spallation through the inhibition of interfacial void formation[49]. It has been suggested that Pt either inhibits S segregation or changes diffusivities in the substrate which, in turn, inhibits the interfacial void formation[50].

The composition of the substrate also appears to affect the performance of the TBC even when covered by a bond coat. Cyclic oxidation of (Ni,Pt)Al/YSZ TBC on Rene N5 at 1150°C showed that both desulfurizing (to 0.7 ppma S) of Rene N5 and the addition of Y in Rene N5 increased the TBC life time[51]. S and Y, presumably, diffuse through the bond coat and affect the scale adhesion. Haynes et al. reported a similar trend of slightly longer TBC life on a desulfurized Re N5 (to 0.9 ppma S), however, Y in Re N5 did not improve the TBC life[52].

There are two sources for the loss Al from the bond coat: the formation of alumina scale and the interdiffusion between the bond coat and the substrate. In terms of bond coat life, the concern is that the Al content in bond coat will prematurely fall below the minimum level required to avoid spinel formation. Equally important, however, is the effect of the influx of Al to the superalloy substrate on the solubility of refractory elements used for strengthening, resulting in precipitation of embrittling phases[53]. Phase transformations due to the Al loss from β-NiAl bond coat on Ni and Ni-16Cr-11Al-Y bond coat on a superalloy substrate at 950°C are illustrated in Figures 2a and 2b, respectively[54].

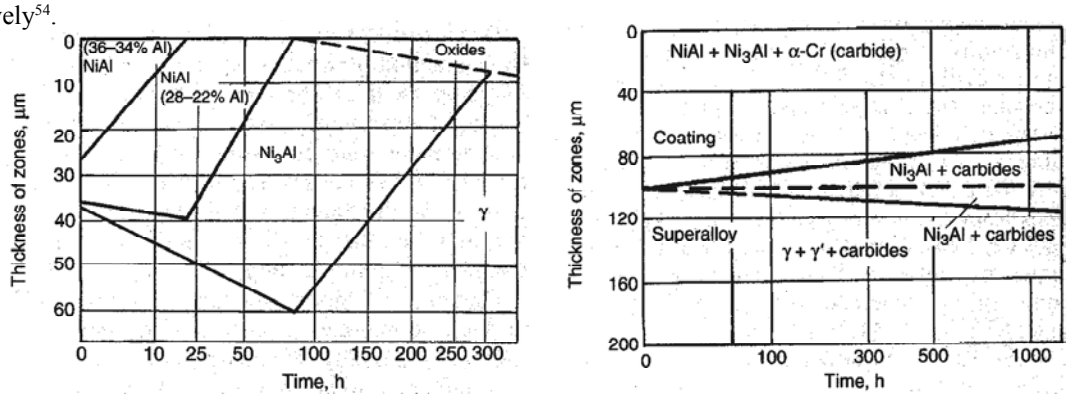

Fig. 2. Phase transformations in (a) β-NiAl bond coat on Ni and (b) Ni-16Cr-11Al-Y bond coat on a superalloy substrate at 950°C (Reprinted with permission of ASM International®. All rights reserved. www.asminternational.org)

Source: See Note 3.

Surface Imperfections

The surface of an initially flat, single phase β-NiAl and (Ni,Pt)Al bond coat on a single crystal superalloy is shown to progressively roughen with thermal exposures[55]. Roughening has also been observed during thermal cycling of MCrAlY coatings on Ni-based superalloys[56]. The most prominent roughening comprises the undulations of the original TBC/bond coat interface[57]. Adherent TGO follows the roughness contour of the bond coat. The surface roughening is far more severe in cyclic exposures compared to isothermal exposures[58].

Phase transformations in bond coat have been suggested as a source for the formation of surface roughening known as 'rumpling'[59]. Two types of phase transformations occur in β-NiAl and (Ni,Pt)Al bond coat during thermal exposures: β to γ' phase and martensite transformation of β phase. The β to γ' phase transformation is due to the depletion of Al from the β phase[60], while the martensite transformation is non-diffusional and shear-dominated transformation[61]. Similar phase transformations are expected to occur in MCrAlY bond coat.

The martensite transformation was observed in bond coats thermally cycled at 1150°C to 5 and 100% of TBC life, suggesting that the transformation accompanied the thermal cycling for most of the TBC life[62]. The volume change for the β to martensite transformation is approximately -2%[63]. Alloys with martensite + γ' structure at room temperature undergo a reversible transformation to single phase β when heated to 1100°C [64]. Bond coat surface rumpling was attributed to the plastic deformation of bond coat caused by the repeated volume changes accompanying the reversible β - martensite phase transformation during thermal cycling[65].

Surface rumpling was also attributed to the volume reduction accompanying the β to γ' phase transformation[66]. The volume reduction can be accommodated by the development of surface recession or by the formation of internal cavities. In the outer part of the bond coat both Ni and Al diffuse toward the surface, therefore there should be a compensating vacancy flux in the opposite direction. The result is expected to be either the formation of Kirkendall porosity or, if the pores collapse, a decrease of the coating volume. It is suggested that the pores tend to collapse during cycling because of thermal stresses in the bond coat, whereas they coalesce into large cavities in isothermal exposures.

Darzens et al. suggest that both the β to martensite and the β to γ' phase transformations contribute to the bond coat and TGO roughness (instability). Figure 3 is a trace of the bond coat/TGO interface at f = 0.76 (fraction of life)[67]. About 70% of the instabilities have the β-phase located at the base. Moreover, there is a greater likelihood that β exists at the base of the most prominent (deepest) instabilities. γ' is present on at least one side of instability with 75% probability, implying that this phase tends to locally impede the TGO displacement. Based on these observations the following mechanism has been suggested[67]. The amplitude of the instability of the TGO has an isothermal and cyclic components, but the latter is appreciably larger. The isothermal component is believed to be associated with the stress caused by the β to γ' transformation. The influence of the transformation on the larger displacements upon cycling appears to involve two effects: (a) the martensite transformation in the β phase results in a volume reduction on cooling larger than in either the γ' or the substrate; (b) γ' has greater strength than the surrounding β at high temperature, impeding the TGO displacement.

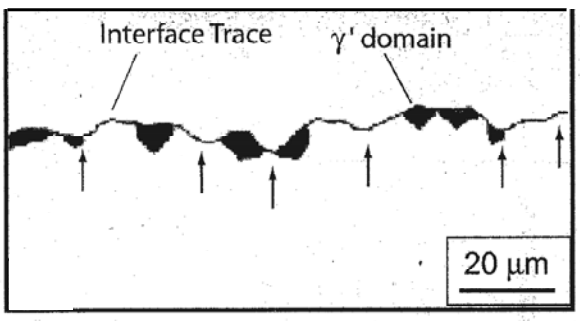

Fig. 3. A trace of the bond coat/TGO interface at f = 0.76 (fraction of life). The arrows designate the base of all large TGO instabilities (Reprinted with permission of TMS. All rights reserved.)

Source: See Note 21. (Darzens, et al.)

Other mechanisms suggested for bond coat imperfections include a thermal 'ratcheting' phenomenon associated with the elastic/plastic mismatch between the bond coat and the growing oxide[68], pre-existing ridge on bond coat grain boundaries and preferential intergranualr oxidation and cracking[69], and Y_2O_3/YAG precipitate phases in MCrAlY bond coat with a columnar morphology acting as preferred channels for rapid inward diffusion of oxygen, causing locally thick regions of TGO[70].

Bond coat imperfections have important implications for TBC performance and failure. Bond coat imperfections cause TGO to displace into the bond coat with each thermal cycle, forming concave regions[71]. The stiffness of the ceramic top coat should constrain the displacement of TGO into the ceramic top cot, preventing the formation of convex regions on the metal surface[72]. The local separations will gradually accumulate on thermal cycling, link together and eventually form the critical sized flaw required for TBC buckling[73].

4.4.2-2c Top Coat

ZrO_2-Based Ceramics

Processing

APS and EB-PVD are the most widely used methods to deposit YSZ top coat on turbine components. Figures 4a and 4b show as-deposited APS and EB-PVD YSZ, respectively. In plasma spraying process, powders of coating material are melted and propelled to the substrate. Upon impingement on the substrate the molten drops are quenched and solidified. A coating is produced by the successive impingement of the drops, referred to as splats, on the substrate. In EB-PVD process, coatings are produced by condensation of vapor on the substrate. A focused electron beam is used to evaporate the coating material. Multiple beams are employed to produce coatings containing components with differing vapor pressures.

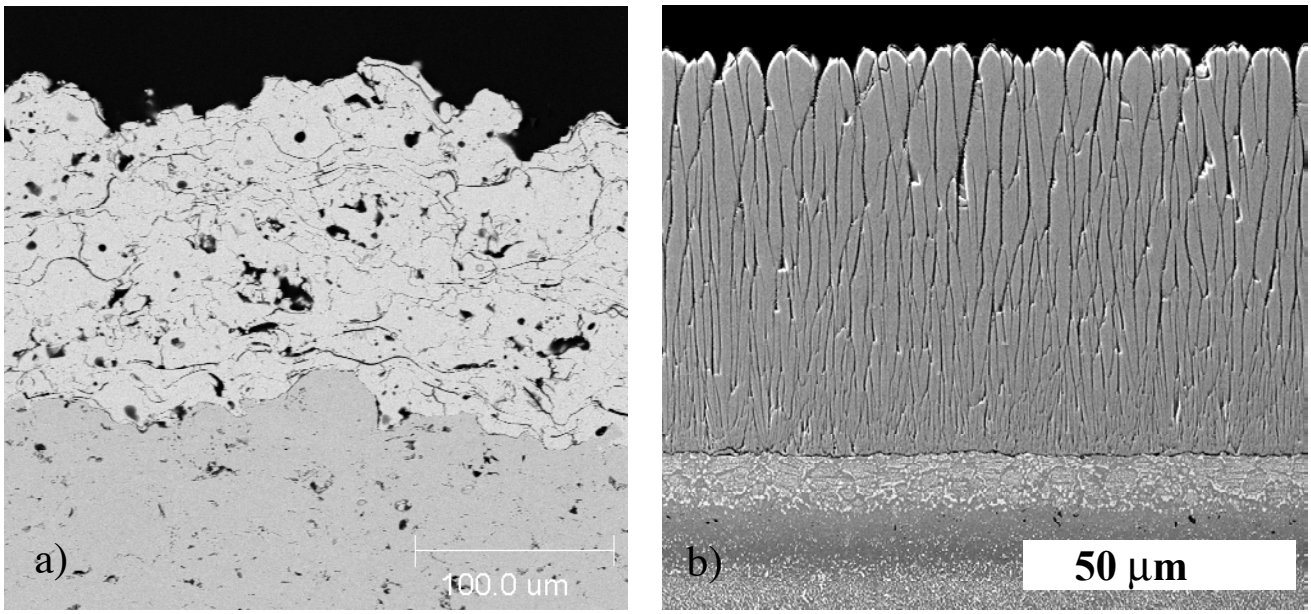

Fig. 4. As-deposited YSZ (7 wt.% Y2O3): (a) APS; (b) EB-PVD

Source: J.I. Eldridge, NASA Glenn Research Center, Cleveland, OH.

APS YSZ has splat structure with inter-splat porosity. Figure 5 is thermal spray coating microstructure showing common features[74]. Two prominent crack morphologies found within as-plasma-sprayed YSZ are[75]: (1) Elongated crack-like separations between flattened splats that melted during the spray deposition. These are oriented nominally parallel to the interface. They form because of thermal contraction as the splats cool; (2) Large, more equi-axed, voids contiguous with equi-axed zirconia particles. These are presumably the particles that did not fully melt during the deposition. The separations between splats are efficient in lowering thermal conductivity, but this is at the expense of surface finish, strain tolerance and erosion resistance[76].

EB-PVD YSZ has a columnar microstructure, which imparts excellent strain tolerance[77], and thus longer cyclic life than APS YSZ. Figure 6 illustrates the dependence of the coating microstructure on the substrate temperature and the rotation speed[78]. Other advantages of EB-PVD YSZ include aerodynamically favorable smooth surface finish and good erosion resistance[79]. But the columnar structure with open porosity parallel to the direction of heat conduction results in a higher thermal conductivity compared to APS YSZ[80].

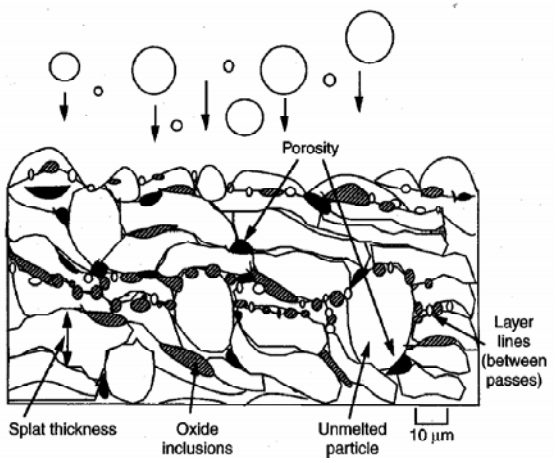

Fig. 5. Thermal spray coating microstructure showing common features (Reprinted with permission of ASM International®. All rights reserved. www.asminternational.org)

Source: See Note 74.

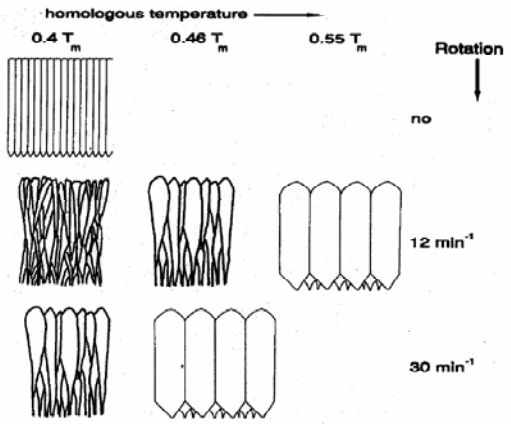

Fig. 6. A schematic illustrating the dependence of the coating microstructure on substrate temperature and rotation speed (Reprinted with permission of Trans Tech Publications. All rights reserved)

Source: See Note 78.

Thermal Conductivity

In thermal barrier coatings, heat is conducted by lattice waves (phonons) as well as by electromagnetic radiation (photons). Lattice waves are elastic or ultrasonic waves, but their spectrum extends to the very high frequencies, where their waves, λ is of atomic dimensions[81]. There are two radiation sources in gas turbine engines: far-field radiation and near-field radiation[82]. Far-field radiation is the radiation from the combustion gas, which is at high temperatures of around 2000°C. Near-field radiation is the radiation from the layer of cooler gas, at around 1200°C, adjacent to the TBC. Radiation can pass through the partially transparent ceramic to the metallic bond coat and substrate. The radiative component of the heat conduction can become a significant portion of the overall thermal conductivity at elevated temperatures. The thermal conductivity by mobile carriers, whether waves or particles, can be expressed in general in the form[83],

$$\kappa = 1/3\ Cvl \qquad (2)$$

where C is the specific heat per unit volume, v is their speed and l is their mean free path. The thermal conductivity is limited by various interaction processes, which transfer energy between the waves[84]. Based on models for thermal conductivity, a low intrinsic thermal conductivity requires weak binding, a large mean atomic weight, a complex crystal structure, non-directional binding and a large number of different atoms per molecule[85].

Lattice imperfections reduce the thermal conductivity by scattering phonons and thereby reducing the mean free path[86]. Point defects, such as solute cations and oxygen vacancies, reduce the lattice thermal conductivity by scattering high-frequency lattice waves, while grain boundaries scatter lattice waves at the low-frequency part of the spectrum. Significant theoretical reductions in the thermal conductivity of YSZ are expected due to grain boundary scattering when the grain sizes are reduced below 100 – 10 nm[87]. These reductions by point defects and grain boundaries are almost independent of each other, since they scatter lattice waves in different frequency ranges.

The effect of yttria dopant level on the thermal conductivity of YSZ was investigated[88]. Thermal conductivity decreased with increasing yttria contents up to 4.5 - 8 mol%. The decrease in thermal conductivity was attributed to a reduced mean free path in zirconia by an increasing phonon scattering, which was likely due to the combined effect of local elastic strain fields generated by incorporating a larger dopant atoms and the introduction of oxygen vacancies into the lattice. The little improvement in the thermal conductivity beyond 4.5 – 8 mol% yttria level was attributed to vacancy clustering[89].

The imperfections which scatter lattice waves have little influence on the radiative component. To reduce this component, one needs larger imperfections, such as porosity and inclusions with almost a micron size[90]. Pores may be preferable, since they present a larger contrast in the index of refraction. Calculations show that the optimum pore diameter is about 0.5 μm for YSZ[91]. An ideal structure for low thermal conductivity has a very fine grain size of nanometer scale, while the matrix contains relatively large inclusions, of the order of 0.5 μm in diameter[92].

Besides photon scattering, porosity decreases the thermal conductivity of a solid by reducing the net-section area through which heat can be transported by phonons and so the reduction in thermal conductivity depends on not only the volume fraction of pores but also their aspect ratio and their spatial distribution[93]. Ideally, flat-pancake shaped pores perpendicular to the temperature gradient, as are formed at splat-boundaries in plasma-sprayed coatings, are most efficient in decreasing the thermal conductivity[94] . The intra-columnar fine porosity in EB-PVD YSZ accounts for the reduced thermal conductivity[95]. This is generally perceived to be much less effective as its distribution generally aligns perpendicular to the coating surface, i.e. parallel to the direction of the primary heat flux[96].

Approaches to Reducing Thermal Conductivity

Alternative Dopants: Doping with ions heavier than yttrium can theoretically decrease the thermal conductivity by increasing the mean atomic weight. Five dopant additions, Er, NiO, Nd, Gd and Yb, were examined with the aim of maximizing lattice strains and lattice anharmonicity[97]. The most effective additions by EB-PVD were Gd, Nd and Yb which resulted in a thermal conductivity of 0.88, 1.00 and 1.02 W/m-K, respectively, calculated for a 4 mol% addition at a coating thickness of 150 µm at 500°C. The thermal conductivity of EB-PVD reference YSZ was ~1.6 W/m-K. Multi-component dopants, ZrO_2-Y_2O_3-Nd_2O_3(Gd_2O_3, Sm_2O_3)-Yb_2O_3(Sc_2O_3), were investigated using a laser rig at 1316°C surface temperature and 950 – 1100°C ceramic/metal interface temperature[98]. The thermal conductivity of APS YSZ (8 wt% or 4.55 mol% Y_2O_3) was about 1 W/m-K, which gradually increased to about 1.4 W/m-K after a 20-h test. In contrast, some ZrO_2-Y_2O_3-Nd_2O_3-Yb_2O_3 or ZrO_2-Y_2O_3-Gd_2O_3-Yb_2O_3 showed thermal conductivity as low as ~0.6 W/m-K, which did not change much after a 20-h test. The thermal conductivity and the rate of thermal conductivity increase were lowest at the total dopant level of 6-13 mol%. The thermal conductivity of EB-PVD ZrO_2-(4-6 mol%)Y_2O_3-Nd_2O_3-Yb_2O_3 was as low as 0.85 W/m-K, while the thermal conductivity of EB-PVD YSZ (8 wt% Y_2O_3) was 1.85-1.9 W/m-K, after a 20-h test. It was proposed that the differing ionic sizes in the solid solution produced distortion, which facilitated the creation of thermodynamically stable, defect clusters that reduced the thermal conductivity and improved sintering resistance[99].

Varying the coating nano-structure: For EB-PVD thermal barrier coatings, the thermal conductivity has been observed to vary with coating thickness[100]. For the early stages of deposition (< 100 µm) a value of 0.8 – 1 W/m-K was reported; however, by the time the coating was 250 µm thick, the mean thermal conductivity was between 1.5 – 1.9 W/m-K at room temperature. Figure 7 shows a two-layer coating approximation consisting of an inner (100 µm) fine-structured zone, overcoated with a layer with thermal conductivity close to bulk YSZ (2.2 W/m-K)[101]. Measurements of the inner, fine-structured grain size gave a value of 3-4 µm, and within each grain was an ultrafine structure of nanometer dimensions. Therefore, renucleation of the EB-PVD coating growth at periodicities less than 100 µm would lower the thermal conductivity[102].

Reduction by layering: Layering offers a promising route to lower the thermal conductivity of an EB-PVD YSZ, which involves the introduction of interfaces/density changes parallel to the YSZ/bond coat interface[103]. A glow discharge plasma was employed to vary the density of YSZ during deposition. The layers were produced by switching the d.c. bias applied to the substrate between high and low levels during deposition. This has the effect of periodically changing the degree of ion bombardment and thus altering the density of the layers produced. Thermal conductivity reduction of the order of 37 – 45% compared to state-of-the-art EB-PVD YSZ has been measured for these layered structures, approaching the values of APS YSZ. The combination of layering at micron dimensions and the introduction of density change from layer to layer work in combination to reduce the thermal conductivity. The layering periodicity is selected to significantly reduce photon transport, while local changes in layer density act to scatter phonons.

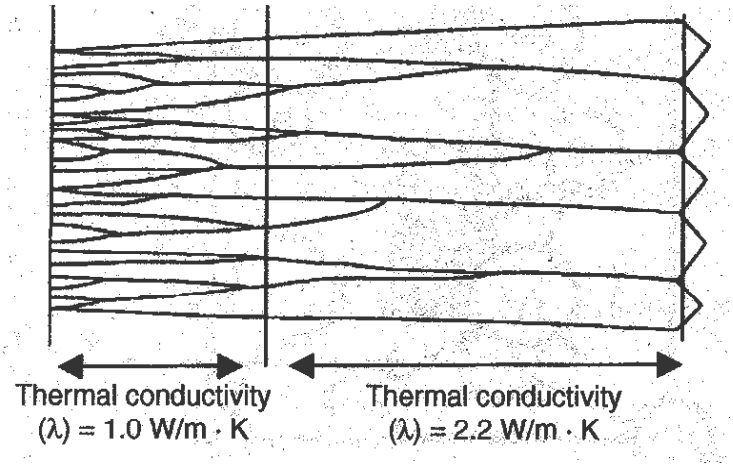

Fig. 7. Schematic of a two-layer coating model, consisting of low conductivity inner layer and a high conductivity outer layer (Reprinted with permission of Trans Tech Publications. All rights reserved)

Source: See Note 101.

Sintering

Sintering leads to an increase in thermal conductivity and thermal stresses. The thermal conductivity of APS YSZ (8 wt.% Y_2O_3) was investigated as a function of time and temperature using a laser rig[104]. The thermal conductivity increased from 1.0 W/m-K to 1.15, 1.19, and 1.5 W/m-K after 30 h at the surface temperature of 990, 1100, and 1320°C, respectively. The increase was attributed to sintering as was evidenced by the decrease in the microporosity. Sintering also increased the hardness and modulus, which increases thermal stresses. The Knoop hardness on the coating surface increased from 4 GPa to 7.5 GPa and the surface modulus increased from 70 GPa to 125 GPa after 120 h at 1100°C.

EB-PVD coatings are more resistant to an increase in thermal conductivity compared to APS coatings. The effect of bond coat surface imperfections on the sintering of EB-PVD YSZ/(Ni,Pt)Al-coated Rene N5 was investigated[105]. On thermal exposure, necks

form and clusters of individual columns sintered together to from large-scale dense regions with large gaps in between, resulting in a 'mud-cracking' pattern. The pattern of the gaps appeared to reproduce the roughness of the underlying bond-coat alloy. The origin of the 'mud-cracking' pattern was attributed to the local undulations in the substrate surface, causing individual columns to converge and narrowing the gap between them. It is thus expected that sintering will be more pronounced on the high-pressure side of blade and on the leading edges than on the low-pressure sides because the surface curvature will tend to cant columns together on the high-pressure side[106]. In practice, the high-pressure side of a blade also tends to be hotter, further likely to promote the sintering.

The influence of the concentration (4-20 mol%) of an alternative dopant Gd_2O_3 on the sintering and grain growth of ZrO_2 solid solutions was investigated[107]. The onset of measurable shrinkage for the ZrO_2-4 mol% Y_2O_3 and ZrO_2-4 mol% Gd_2O_3 occurred at ~1100 and ~1175°C, respectively. The shrinkage at a given temperature increased as the Gd_2O_3 content increased to 8 mol% but then decreased for higher Gd_2O_3 concentration. The grain size data showed a trend similar to the sintering data: the average grain size showed a maximum at a Gd_2O_3 concentration of 8 mol%. The slower thermal conductivity increase on thermal aging for ZrO_2 alloyed with multi-component dopants Y_2O_3-Nd_2O_3(Gd_2O_3, Sm_2O_3)-Yb_2O_3(Sc_2O_3)[108] was presumably due to reduced sintering. It appears that heavy rare earth oxide dopants are effective in reducing the sintering of ZrO_2 solid solutions.

Phase Transformation

The excellent phase stability of YSZ is due to the formation of the metastable, nontransformable *t*' phase which is very stable at temperatures below ~1200°C[109]. The phase stability of plasma-sprayed YSZ (8.6 mol% Y_2O_3) was examined by XRD[110]. The as-sprayed YSZ was primarily a nontransformable tetragonal phase (*t*'), having about the same composition as the starting powder. The formation of the nontransformable tetragonal phase (*t*') is due to the rapid quench in the process. Figure 8 shows the mole fraction of phases versus temperature after 100-h aging[111]. Aging at 1200 and 1400°C progressively increased the amounts of equilibrium cubic (*c*) and transformable tetragonal (*t*) phases at the high temperature and this resulted in cubic (*c*) and monoclinic (*m*) phases at room temperature. The yttria content of the remaining *t*' phase was lowered to ~ 5 mol% after 100 h at 1400°C. The *t* to *m* phase transformation on cooling with its accompanying volume expansion can lead to disintegration of the coating[112]. In laboratory torch tests, regions of optimal TBC lives were found to correlate with regions having high amounts of the *t*' phase, small but nonzero amounts of the *m* phase, and little or no *c* phase[113].

EB-PVD YSZ (7 wt.% Y_2O_3) was investigated in regard to phase transformation after annealing[114]. Free-standing YSZ was heat-treated in air, for up to 200 h, in the temperature range 1200 – 1400°C. For 6-8 wt.% EB-PVD YSZ, the equilibrium phase diagram[115] predicts a two-phase mixture, consisting of *t* phase containing 4 wt.% Y_2O_3 and *c* phase containing 16 wt.% Y_2O_3, at the deposition temperature of ~1000°C. The *t*' phase, however, forms due to the rapid quench in the process. Annealing for short times (10 h at 1400°C and 30 h at 1300°C) and longer times at 1200°C produced significant amount of *m* phase, reaching ~ 20 mol% after 100 h at 1400°C. The proportion of *c* phase increased rapidly for all annealing conditions (1200 – 1400°C); at 1400°C, the content of *c* phase increased to ~55 mol% as soon as the temperature was reached and remained at that level up to 100 h. In general, the transformation to the *c* phase was more rapid than the transformation to *m* phase.

Schultz et al. report that EB-PVD TBCs were stable up to 100 h at 1150°C, but transformed to a mixture of t+c+m phases after annealing for 100 h at 1400°C[116]. A slower cooling rate increased the amount of m phase at room temperature[117]. For instance, after 100 h at 1371°C, the amount of m phase increased from < 10 mol% to > 30 mol% when slow furnace cooling was used instead of quenching. Overall, the amount of m phase was in the same range for EB-PVD and APS coatings when aged in a similar condition[118].

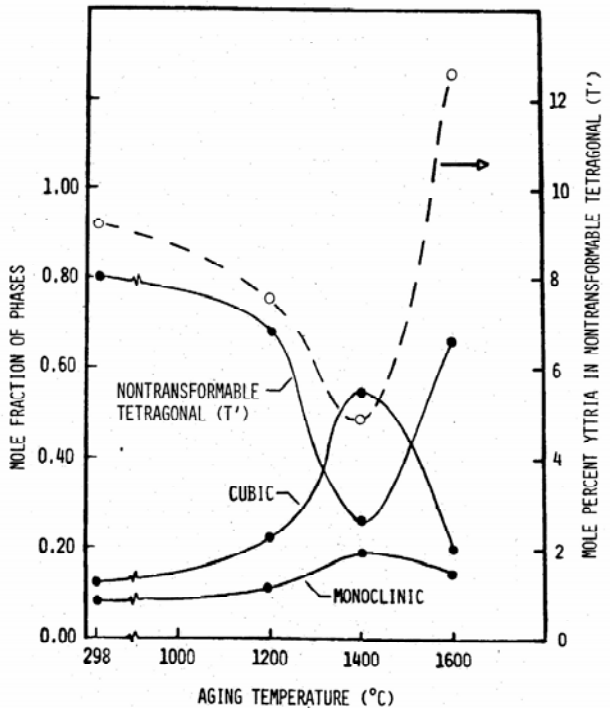

Fig. 8. Plot of the mole fraction of phases versus temperature for a 100-h aging (Reprinted with permission of The American Ceramic Society, copyright 1981, www.ceramics.org)

Source: See Note 23.

Alternative Coating Materials

Zirconates

Rare earth zirconates are being explored as alternate TBC materials. Rare earth zirconates, $M_2Zr_2O_7$ (M = rare earth element), crystallize in the ordered pyrochlore structure over a composition range[119]. At elevated temperatures and outside the composition range, the disordered fluorite structure is the stable phase[120]. Maloney proposed the use of $M_2D_2O_7$ (M = Gd, La, Y; D = Hf, Ti, Zr) as TBCs, while Suresh et al. independently proposed the use of a much broader family of compounds, where M represents all elements from the lanthanide series (La to Yb)[121].

The thermal conductivity of hot-pressed $Gd_2Zr_2O_7$, $Nd_2Zr_2O_7$, and $Sm_2Zr_2O_7$ was investigated at 25-700°C[122]. The thermal conductivity of $Gd_2Zr_2O_7$, $Nd_2Zr_2O_7$ and $Sm_2Zr_2O_7$ at 700°C was 1.6, 1.6 and 1.5 W/m-K, respectively, which was about 30% lower than the thermal conductivity of the reference YSZ (2.3 W/m-K). The decrease was attributed to phonon scattering by point defects. The two types of point defects expected in these materials are substitutional rare-earth solute cations (Gd, Nd, and Sm) replacing zirconium and the corresponding oxygen vacancies created by the substitution of tetravalent zirconium by trivalent rare-earth element[123]. The scattering strength of oxygen vacancies is larger than that of substitutional solutes, because of the missing anion mass and the missing interatomic linkages associated with the vacancies. The lower thermal conductivity compared to YSZ was attributed to two factors[124]: (i) higher concentration of oxygen vacancies present, and (ii) more effective phonon scattering by solute cations as a result of the significant atomic weight difference between the cations and zirconium.

Two perovskites ($SrZrO_3$ and $BaZrO_3$) and one pyrochlore ($La_2Zr_2O_7$) were investigated as TBC candidates[125]. Sintered $SrZrO_3$ cracked ~600°C which was attributed to the volume change due to a phase transformation, making it unsuitable for a TBC. At 1000°C, the thermal conductivity of sintered $BaZrO_3$ and $La_2Zr_2O_7$ was 3.4 and 1.6 W/m-K, respectively, while the thermal conductivity of sintered YSZ was ~2.2 W/m-K. The Young's modulus and hardness of sintered $BaZrO_3$ and $La_2Zr_2O_7$ were ~15% lower than those of sintered YSZ, while the CTEs were slightly lower than that of YSZ up to 1400°C. Low Young's modulus is beneficial to thermal stresses, while low CTE is detrimental to thermal stresses. Plasma-sprayed $La_2Zr_2O_7$ performed better than $BaZrO_3$ in thermal cycling[126]. However, the $La_2Zr_2O_7$ coating had a significantly shorter life than the YSZ coating, by roughly an order of magnitude in thermal cycling at 1240-1360°C[127] . Layered or graded coatings with YSZ as the first ceramic coating of the TBC system and $La_2Zr_2O_7$ as the final topcoat showed much improved performance, showing lives similar to YSZ[128].

Yttria-Stabilized HfO_2

Replacing the Zr in YSZ with Hf can theoretically decrease the thermal conductivity by increasing the mean atomic weight. Plasma-sprayed hafnia-yttria coatings (HfO_2-8.4 wt.% Y_2O_3, HfO_2-11.4 wt.% Y_2O_3, HfO_2-15.0 wt.% Y_2O_3, HfO_2- 27.2 wt.% Y_2O_3) were evaluated with respect to plasma-sprayed YSZ (6-9 wt.% Y_2O_3) in a burner rig[129]. The hafnia-yttria coatings were very sensitive to plasma-spray parameters and high-quality coatings were obtained only when specific parameters were used. In contrast, YSZ coatings were in general relatively insensitive to spray parameter variations. In contrast to zirconia-yttria compositions, the hafnia-yttria compositions with the fully stabilized cubic phase (HfO_2- 27.2 wt.% Y_2O_3) outperformed the partially stabilized compositions. The fully stabilized hafnia-yttria performed about as well as the YSZ coating when sprayed with certain parameter sets. It is possible that the fully stabilized hafnia-yttria may be more stable at higher temperatures (>1200°C) than the partially stabilized YSZ. The HfO_2-27.2 wt.% Y_2O_3 also showed significantly superior resistance to sintering compared to YSZ (8 wt.% Y_2O_3) after 15 h at 1400°C.

YAG

The thermal conductivity of dense, polycrystalline yttrium-based garnets in the temperature range 23 – 1000°C was investigated[130]. The high-temperature thermal conductivity of these garnets was in the range 2.4 – 3.2 W/m-K, which is somewhat higher than the thermal conductivity of dense YSZ (~2.4 W/m-K). It was demonstrated that the thermal conductivity of these garnets could be tailored by forming substitutional solid solution alloys. The oxygen diffusivity of YAG is about 10 orders of magnitude lower than that in zirconia, suggesting its potential as an alternative to zirconia in future TBCs for improved durability.

4.4.2-2d Failure Mechanisms of TBC

While there are several different ways in which TBCs can fail, the mechanisms of greatest concern are those that intimately involve the growth of the TGO[131]. The failure is governed by a sequence of crack nucleation, propagation and coalescence events along the bond coat/TGO or top coat/TGO interfaces[132]. Figure 9 schematically illustrates the cracking sequence by growth misfit, followed by cooling to ambient[133]. Eventual failure occurs by either buckle, or edge-driven delamination[134], with a failure plane located at (or near) the interface between the TBC and the bond coat. The life of specific system appears to correlate with the average thickness of the TGO[135].

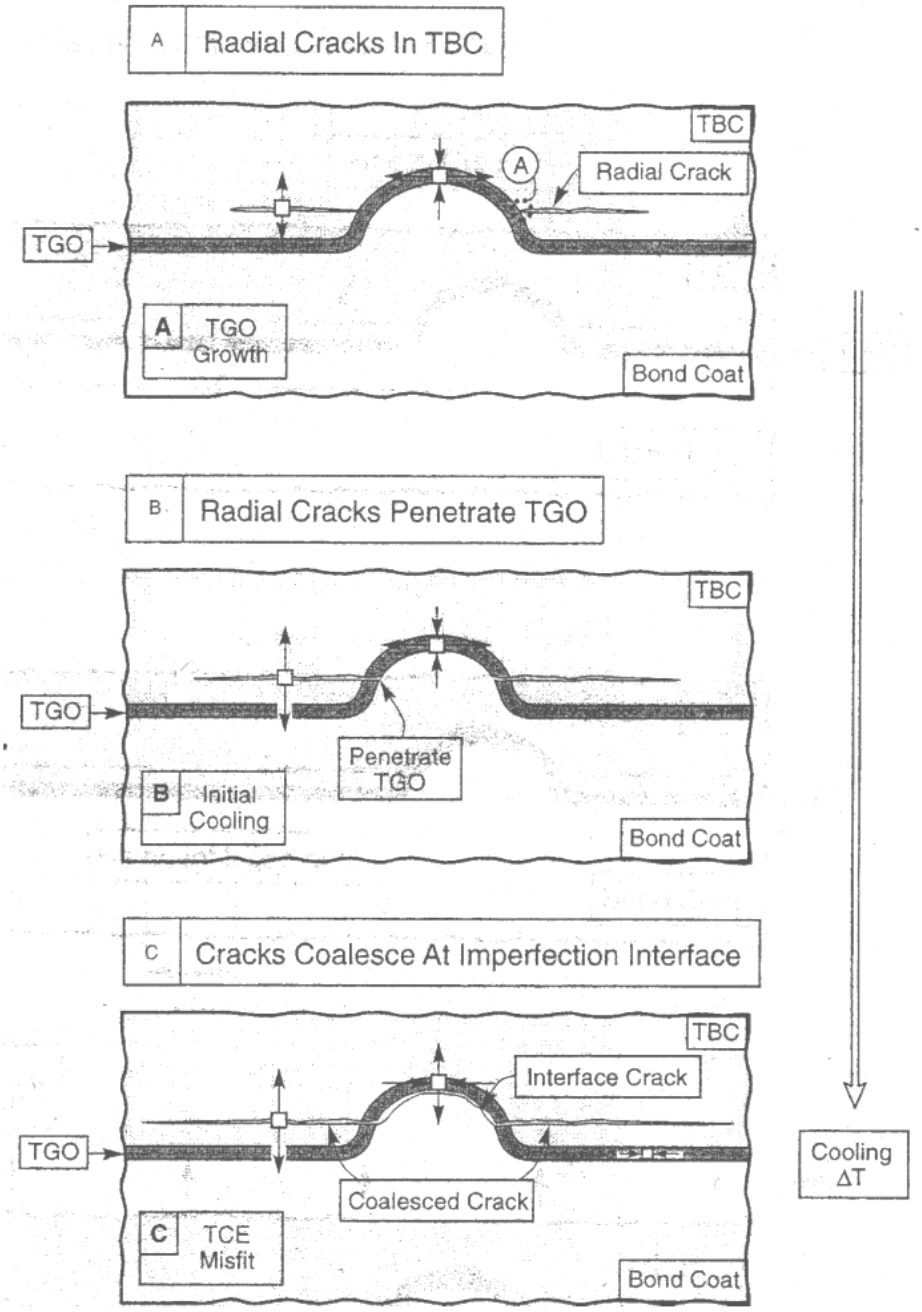

Fig. 9. Schematic illustration of the cracking sequence by growth misfit, followed by cooling to ambient (Reprinted with permission of Elsevier, copyright 2000.)

Source: See Note 34.

APS

The separation that nucleates the failure sequence appears to be associated with imperfections at (or near) the interface between the TBC and bond coat[136]. The most prominent are undulations in the original bond coat surface. The trajectory of the delamination that causes final failure resides primarily within the TBC itself and connects the peaks of the undulations. Rabiei & Evans suggest the following failure mechanism[137]. The sources of stress are those formed upon TGO growth, followed by the changes that happen because of thermal expansion misfit on cooling to ambient. The zones that experience out-of-plane tensile stress are most important, since these are the stresses responsible for nucleating and propagating cracks along delamination planes in the system. See Figure 9 for the cracking sequence. Radial cracks form in the TBC as the TGO thickens because of the out-of-plane stress in the TBC normal to the interface. The TBC cracks do not penetrate to TGO because the interface between the TGO and bond coat is in compression. On cooling to ambient, the CTE misfit causes appreciable tension to develop normal to the interface between the TGO and bond coat and this interface separates. The coalescence of this separation with the radial cracks in the TBC, by rupturing the intervening TGO, is a key event. Once coalescence happens, the energy density available in the TGO attached to the upper portion of the crack becomes available for outward growth of the crack in the TBC.

EB-PVD

The most crucial constituents for the failure of EB-PVD TBC are[138]: (i) Imperfections in the TGO affect the TBC life; (ii) The failure occurs by large scale buckling (LSB), subject to the development of large separated domains at the interface. Life is governed by the evolution of these separations up to the critical size needed for LSB; (iii) The adhesion of the TGO/bond coat interface degrades upon thermal exposure, both because of embrittlement by segregants and the growth of separations around the imperfections in the TGO. Mumm and Evans suggest the following mechanism[139]. As the TGO thickens with extended elevated temperature exposure, imperfections develop and enlarge. Accordingly, the ambient temperature energy release rate around the imperfections becomes larger the longer the exposure. There may be simultaneous, time-dependent embrittlement of the TGO/bond coat interface, perhaps by S segregation. When the imperfections become large enough, interface separations nucleate in their vicinity. An appreciable energy release rate develops only on cooling, caused by the CTE misfit between the TGO and the superalloy. Separations should from only on cooling. After longer exposures, when the imperfections further enlarge, it is surmised that some of the separations coalesce. The trajectory of the delamination primarily occurs at the TGO/bond coat interface.

4.4.2-3a Coatings for Ceramic Components

Key requirements for a successful EBC include[140]: i) environmental stability, especially in water vapor; ii) coefficient of thermal expansion (CTE) match; iii) chemical compatibility; and iv) phase stability. It is also desirable to have a low thermal conductivity for maximum thermal insulation capability. Table I compares the CTE of SiC, Si_3N_4, and current EBC materials[141]. Note the good CTE match between Si-based ceramics and EBC materials .

Table I. CTE of Si-based ceramics and current EBC materials

Material	SiC	Si_3N_4	Si	Mullite*	BSAS**	Y_2SiO_5	Sc_2SiO_5	Er_2SiO_5	Yb_2SiO_5
CTE (10^{-6}/C)	4.5 ~ 5.5	3 ~ 4	3.5 ~ 4.5	5 ~ 6	4 ~ 5	5 ~ 6	5 ~ 6	7 ~ 8	7 ~ 8

* $3Al_2O_3{\cdot}2SiO_2$

** $1\text{-}xBaO{\cdot}xSrO{\cdot}Al_2O_3{\cdot}2SiO_2$, $0 \le x \le 1$

Source: See Note 141.

Table II lists the thermal conductivity of hot-pressed EBC materials determined by a high heat flux laser rig at 200°C - 1400°C[142]. Mullite ($3Al_2O_3{\cdot}2SiO_2$) and BSAS ($1\text{-}xBaO{\cdot}xSrO{\cdot}Al_2O_3{\cdot}2SiO_2$, $0 \le x \le 1$) have thermal conductivities similar to that of YSZ (8 wt.% Y_2O_3), while rare earth monosilicates, except for Sc_2SiO_5, have lower thermal conductivities than YSZ.

Table II. Thermal conductivity of hot-pressed current EBC materials at 200°C - 1400°C determined by a high heat flux laser rig

Material	YSZ	Mullite	BSAS	Mullite +BSAS	Y_2SiO_5	Sc_2SiO_5	Yb_2SiO_5	Er_2SiO_5
Thermal conductivity (W/m-k)	2.2 ~ 2.9	2.2 ~ 2.8	2.5 ~ 3.0	2.0 ~ 2.3	1.6 ~ 1.9	2.3 ~ 3.5	1.3 ~ 1.4	1.4 ~ 1.5

Source: See Note 142.

Current EBCs have multi layers designed in such a way that the system satisfies all the key requirements for a successful EBC. They consist of a silicon bond coat and a ceramic top coat. The ceramic top coat typically comprises at least two ceramic layers. The bond coat facilitates the adherence of the ceramic top coat to the substrate and the ceramic top coat provides protection from water vapor and thermal insulation.

4.4.2-3b Processing

APS is the most successful and widely used process to apply EBCs[142]. With EB-PVD process, the low vapor pressure of silica compared to alumina and rare earth oxides makes it difficult to produce coatings with the desired stoichiometry. Other coating processes being explored include chemical vapor deposition (CVD)[143], sol-gel, and slurry coatings[144], which have the benefit of being none-line-of-sight processes.

4.4.2-3c Testing

The key component in EBC testing is water vapor. Laboratory scale high steam rigs[145] are used to simulate the high water vapor pressure, while high pressure/high velocity burner rigs[146] are used to simulate both the high water vapor pressure and high gas velocity. A low gas velocity (a few cm/sec) is typically employed in laboratory scale high steam rigs due to the simplicity. Since water vapor is the most critical factor that affects the performance of EBCs, this test is suitable for the initial screening of EBC candidates and for the evaluation of long-term EBC performance. The high pressure/high velocity burner rig test is suitable for proof tests of mature EBCs and for subcomponent tests since it closely simulates actual gas turbine environments. Burner rigs can be set up to generate a temperature gradient through the EBC, simulating the temperature profile of cooled components. Laser rigs are used for thermal conductivity measurements as well as for the evaluation of EBC performance under a temperature gradient[147].

4.4.2-3d Bond Coat

Silicon is the current bond coat. It provides excellent durability to EBC by facilitating adherence to the ceramic top coat and the oxidation resistance[148]. The excellent performance of Si bond coat is attributed to its close CTE match with Si-based ceramics, oxidation resistance due to the formation of slow-growing silica scale and chemical compatibility with the substrate and the ceramic top coat. The use of silicon bond coat is limited by its melting point (~1416°C). For higher temperature applications where Si bond coat melts, the next ceramic layer, such as a mullite-based coating, becomes the bond coat. The life of EBC is significantly reduced without Si bond coat.

4.4.2-3e Top Coat

Current top coat can be divided into two groups, i.e. top coat with a mullite-based layer and top coat without a mullite-based layer. Table III lists the current top coats.

Table III. List of current top coats

With a mullite-based layer	Without a mullite-based layer
mullite mullite + BSAS mullite or mullite + BSAS / YSZ mullite or mullite + BSAS / BSAS mullite or mullite + BSAS / RE_2SiO_5 or $RE_2Si_2O_7$*	BSAS RE_2SiO_5* $RE_2Si_2O_7$* Ta_2O_5

* RE: rare earth element

Top Coat with a Mullite-Based Layer

Mullite has attracted the most interest as a protective coating for Si-based ceramics because of its good CTE match and chemical compatibility with SiC and Si_3N_4 ceramics[149]. With the emergence of Si bond coat, mullite and mullite-based coatings became an intermediate layer bridging the Si bond coat and the water vapor-resistant top layer[150]. Key functions of mullite-based coatings when used as an intermediate coat in current EBCs include chemical compatibility, strain tolerance, and barrier to water vapor transport.

Mullite and Mullite+BSAS

Conventionally plasma-sprayed mullite coatings contain a significant amount of metastable amorphous phase due to the rapid cooling of molten mullite during the solidification on a cold substrate[151]. A subsequent exposure of the mullite coating to a temperature above ~1000°C causes the crystallization of the amorphous phase. Shrinkage accompanies the crystallization, leading to cracking and delamination of the mullite coating. A modified plasma-spraying process enables the deposition of crystalline mullite coating, dramatically improving the crack resistance and adherence[152]. Plasma-sprayed mullite coating on SiC remained virtually intact at the mullite/SiC interface as well as on the mullite surface after a 50-h exposure in a high pressure (6 atm) hot corrosion rig containing Na_2SO_4[153]. CVD mullite also displayed little evidence of damage in Na_2SO_4 environments[154]. Further improvement in the crack resistance of plasma-sprayed mullite coatings is achieved by adding a second phase (BSAS)[155]. The improved crack resistance of the mullite+BSAS composite coating is attributed to the reduced coating tensile stress due to the low modulus BSAS phase[156].

Mullite/YSZ

The relatively high silica activity of mullite (0.3 ~ 0.4) causes the selective volatilization of silica and the recession of mullite in high velocity combustion environments[157]. Therefore, a water-vapor resistant overlay coating is needed on top of the mullite coating, to provide the stability in water vapor. YSZ is a logical candidate for a top coat because it has been successfully used as a TBC for superalloy components in gas turbine engines, signifying its stability in water vapor. The mullite/YSZ system is an effective EBC for short term exposures. One critical disadvantage of YSZ is the high CTE and sintering. The stresses due to the CTE mismatch and sintering cause severe cracking. These cracks provide easy paths for water vapor penetration, resulting in rapid oxidation and premature coating delamination[158].

Mullite/BSAS and Mullite+BSAS/BSAS

BSAS is a top coat material developed in the NASA's High Speed Research-Enabling Propulsions Materials (HSR-EPM) program in joint research by NASA, General Electric, and Pratt and Whitney[159]. It has the key attributes for a successful EBC, such as a low silica activity, a low CTE, and a low modulus (~100 GPa for dense BSAS). The low silica activity provides stability in water vapor, while the low CTE and low modulus provide low thermal stresses. The EPM EBCs exhibit dramatically improved durability compared to the mullite/YSZ EBC. Figure 10 shows plasma-sprayed Si/mullite+20 wt.% BSAS/BSAS on SiC/SiC composite after 1000 h at 1316°C (1-h cycles) in 90% H_2O-balance O_2[160]. The EBC maintained excellent adherence and crack resistance. Pockets of glasses developed within the BSAS top coat. The EPM EBC was applied on SiC/SiC composite combustor liners in Solar Turbines (San Diego, CA) Centaur 50s gas turbine engines under DOE Ceramic Stationary Gas Turbines (CSGT) Program[161]. One engine used by Texaco in Bakersfield, CA, successfully completed a 14,000-h field test (~1,250°C maximum combustor liner temperature). The higher operating temperature resulted in emissions consistently below 15 ppmv nitrogen oxides (NOx) and below 10 ppmv carbon monoxide (CO) throughout, roughly reducing the NOx and CO loads on the environment by factors of about 2 and 5, respectively.

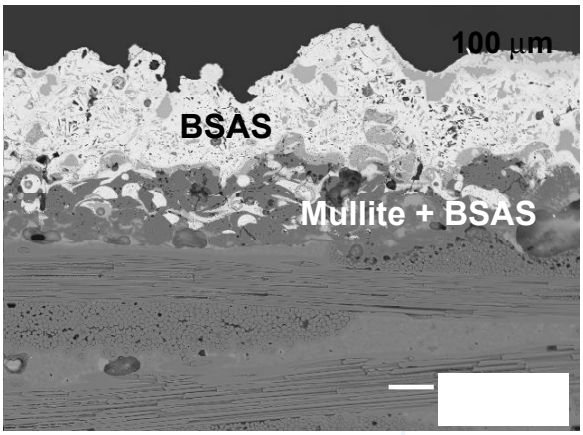

Fig. 10. Plasma-sprayed Si/mullite+20 wt.% BSAS/BSAS on a SiC/SiC composite coupon after 1000 h at 1316°C (1-h cycles) in 90% H2O-balance O2 (Reprinted with permission of Elsevier, copyright 2005)

Source: See Note 141.

The EPM EBCs have some durability issues that limit their upper use temperature and life[162]. One key issue is the volatilization of the BSAS top coat in high velocity combustion environments. A projection based on a silica volatility model in conjunction with BSAS volatility data indicates a BSAS recession of ~70 μm after 1000 h at 1400°C, 6 atm total pressure and 24 m/s gas velocity. Actual gas turbines operate at significantly higher pressures and gas velocities, which increases the projected recession to much higher levels. The EBC in Solar Turbines engines suffered significant BSAS recession in some areas after the 14,000-h test[163]. Another key issue is the chemical reaction between BSAS and the thermally grown silica on Si bond coat. The BSAS-silica reaction produces a low-melting (~1300°C) glass that causes EBC degradation and a premature failure at temperatures above ~1300°C. The pockets of glasses in Figure 10 are due to the BSAS-silica reaction. Therefore, it is desirable to avoid the BSAS second phase in the mullite layer for applications requiring long-term exposures at temperatures above 1300°C ~ 1350°C.

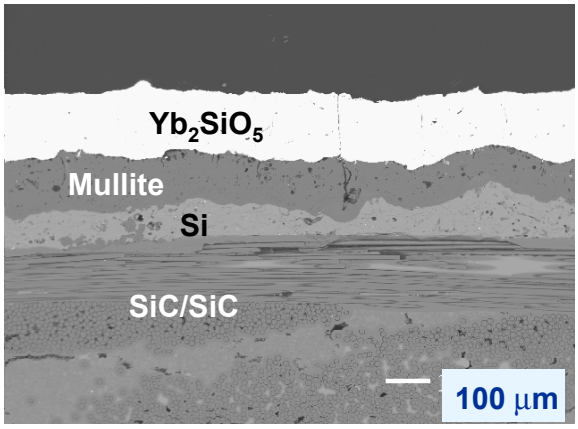

Fig. 11. Plasma-sprayed Si/mullite/Yb2SiO5 on SiC/SiC composite after 1000 h at 1380°C (1-h cycles) in 90% H2O-balance O2. (Reprinted with permission of ASM International, All rights reserved, www.asminternational.org)

Source: See Note 142.

Mullite/RE_2SiO_5 (or $RE_2Si_2O_7$) and Mullite+BSAS/RE_2SiO_5 (or $RE_2Si_2O_7$)

Some rare earth silicates have a low CTE, phase stability, and a low silica activity, making them excellent EBC top coat materials[164]. Volatility data[165] and thermodynamic calculations[166] indicate that rare earth monosilicates (RE_2SiO_5; RE = rare earth element) are significantly less volatile than BSAS in water vapor, at least by an order of magnitude, while the volatilities of rare earth disilicates ($RE_2Si_2O_7$) are similar to that of BSAS. Disilicates of Y, Yb, and Lu exposed to a high velocity and high steam environment at 1450°C ~ 1500°C gradually decomposed to Y_2SiO_5, Yb_2SiO_5, and Lu_2SiO_5, respectively, indicating the selective volatilization of silica[167].

Figures 11 and 12 show plasma-sprayed Si/mullite/Yb_2SiO_5 on SiC/SiC composite (1000 h) and on Si_3N_4 (400 h) at 1380°C (1-h cycles) in 90% H_2O-balance O_2[168]. The EBC maintained superb adherence and crack resistance on both substrates. In contrast, plasma-sprayed Si/mullite/YSZ on Si_3N_4 suffered severe cracking and delamination after 280 h at 1380°C (1-h cycles) in 90% H_2O-balance O_2 (Figure 13)[169]. This demonstrates the detrimental effect of a large CTE mismatch between EBC and substrate. Figure 14 shows plasma-sprayed Si/mullite/Yb_2SiO_5 on SiC/SiC composite after 100 h in a high pressure/high velocity burner rig (1400°C, 100 h, 6 atm, gas velocity = 24 m/s)[169]. Note the excellent adherence, crack resistance, and oxidation resistance of the rare earth silicate EBC in a simulated gas turbine environment.

Top Coat without a Mullite-Based Layer

BSAS and RE_2SiO_5 possess key properties desirable for a successful EBC, such as low CTE, low silica volatility, and phase stability[170]. Ta_2O_5 has a low CTE, but relatively high volatility in water vapor, higher than the volatility of BSAS by an order of magnitude[171], and a phase transformation at ~ 1370°C. The performance of these materials without a mullite-based intermediate layer was investigated.

BSAS

BSAS is reactive with silica, thermally grown on SiC or Si_3N_4, forming a low melting eutectic (mp ~ 1300°C). The chemical reaction causes the build-up of a thick reaction zone and porosity at the BSAS/substrate interface. Plasma-sprayed BSAS-coated SiC/SiC composite after 100 h (2-h cycles) at 1300°C in 90% H_2O - balance O_2 developed a thick (~20 μm) reaction zone and large pores at the BSAS/substrate interface[172]. Pores are attributed to the bubbling of gaseous species through the low viscosity eutectic glass. In long-term exposures, the pores continue to grow and coalesce, leading to complete coating spallation. The low viscosity reaction zone can lead to the EBC spallation under a high shear stress. Similar behavior is observed in the presence of Si bond coat.

RE_2SiO_5, $RE_2Si_2O_7$, and Ta_2O_5

Plasma-sprayed RE_2SiO_5[173] and Ta_2O_5-based[174] EBCs showed good adherence on Si-based ceramics under thermal exposures in air. However, these coatings on SiC/SiC composite did not maintain the adherence in water vapor environments[175]. Consequently, the substrate suffered rapid oxidation, forming thick and porous scale. A premature EBC spallation occurred along the scale since the thick scale constituted a weak mechanical link. Possible explanations for the rapid oxidation include lack of chemical bonding and EBC cracking under thermal cycling. Both can provide an easy access for water vapor into the interface. The fact that the Si/mullite EBC shows far superior oxidation resistance and longer life, although mullite develops similar cracks, suggests that inadequate chemical bonding may be responsible for the lack of oxidation resistance. Other low CTE rare earth monosilicates, such as Y_2SiO_5, Er_2SiO_5, Sc_2SiO_5, and Lu_2SiO_5, exhibited similar poor oxidation resistance[176]. CVD Ta_2O_5 was unstable in an environment containing Na_2SO_4, rapidly reacting to form $NaTaO_3$ which subsequently interacted destructively with the underlying Si_3N_4 substrate to form a molten phase[177]. Rare earth disilicates ($RE_2Si_2O_7$) were applied on Si_3N_4 ceramics by a slurry process followed by sintering[178]. Short-term exposures at relatively low temperatures showed promising results, indicating their merits for further research.

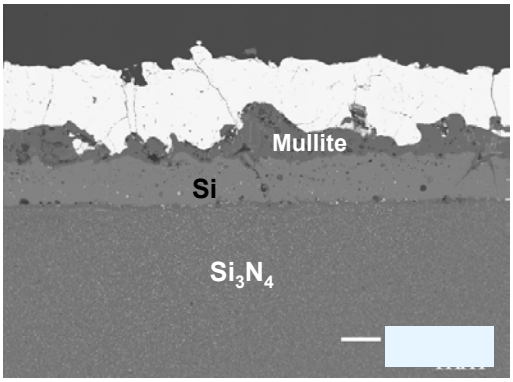

Fig. 12. Plasma-sprayed Si/mullite/Yb2SiO5 on Si3N4 after 400 h at 1380°C (1-h cycles) in 90% H2O-balance O2. (Reprinted with permission of Elsevier, copyright 2005.)

Source: See Note 141.

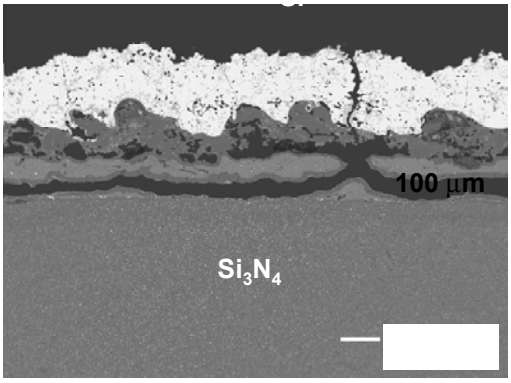

Fig. 13. Plasma-sprayed Si/mullite/YSZ on Si3N4 after 280 h at 1380°C (1-h cycles) in 90% H2O-balance O2.

Source: See Note 169.

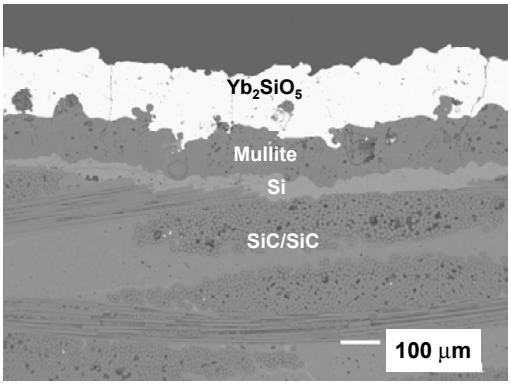

Fig. 14. Plasma-sprayed Si/mullite/Yb2SiO5 on a SiC/SiC composite after 100 h in a high pressure/high velocity burner rig (1400°C, 100 h, 6 atm, gas velocity = 24 m/s).

Source: See Note 169.

4.4.2-4 Conclusions

Thermal barrier coatings for superalloys and environmental barrier coatings for ceramic matrix composites are important technologies to achieve higher gas turbine inlet temperatures.

In thermal barrier coatings, stresses play the major role in coating failure, which are influenced by various factors such as bond coat oxidation, bond coat surface roughening, YSZ phase transformation, and YSZ sintering. Current approaches for improvements include adding reactive element (RE) or precious metals in the bond coat for enhanced oxidation resistance, and alternative oxide stabilizers for ZrO_2 and alternative materials to ZrO_2 for enhanced phase stability and sinter resistance. Thermal conductivity is another key element for the TBC performance. A lower thermal conductivity TBC lowers the substrate temperature and/or reduces the TBC thickness, which improves the performance and life of gas turbine components. Key future research areas include the development of new bond coat alloy compositions resistant to surface imperfections and the development of low thermal conductivity TBC, without compromising the quality of TGO and TBC life.

In environmental barrier coatings, chemical reactions, rather than stresses, appear to play the major role in the coating degradation. Key life-limiting reactions are water vapor volatility of the surface layer, chemical reactions between various EBC layers, including silica TGO, and the oxidation of silicon bond coat. Therefore, it is important to design EBC in such a way to minimize these chemical

reactions. The selection of an EBC for a particular system depends on application requirements, such as the EBC surface temperature, the substrate temperature, and the life goal. Alternative top layer materials to BSAS are being investigated for applications at T>1300°C. Rare earth silicates have shown promising results, while ZrO_2- and HfO_2-based materials require further research to alleviate the thermal expansion mismatch stress.

As advanced gas turbines rely on these coatings for environmental/thermal protection, life models to predict the remaining coating life and non-destructive technologies to monitor the coating's health are important future research areas.

4.4.2-5 Notes

1. F.O. Soechting, Thermal Barrier Coating Workshop, NASA Lewis Research Center, Cleveland, OH, NASA Conference Publication 3312, (1995): 1-15.
2. M. J. Donachie and S. J. Donachie, Superalloys – Second Edition, ASM International, Materials Park, Ohio (2000).
3. Y. Tamarin, Protective Coatings for Turbine Blades, ASM International, Materials Park, OH (2002).
4. Ibid.
5. Ibid.
6. See note 1 above.
7. R. A. Miller, Thermal Barrier Coating Workshop, NASA Lewis Research Center, Cleveland, OH, NASA Conference Publication 3312 (1995): 17-34.
8. D. Anson and D. W. Richerson, Progress in Ceramic Gas Turbine Development, Vol. 2. Edited by M. van Roode, M. Ferber, and D. W. Richerson, ASME PRESS, New York, NY, 1-10 (2003).
9. N. S. Jacobson, J. Am. Ceram. Soc., 76[1] (1993): 3-28.
10. E. J. Opila and R. Hann, J. Am. Ceram. Soc., 80[1], 197-205 (1997); J. L. Smialek, R. C. Robinson, E. J. Opila, D. S. Fox, and N. S. Jacobson, Adv. Composite Mater., 8[1] (1999): 33-45.
11. N. S. Jacobson, J. L. Smialek, and D. S. Fox, Handbook of Ceramics and Composites, Vol. 1. Edited by N. S. Cheremisinoff, Marcel Dekker, New York, NY, USA, 99-135 (1990).
12. K. N. Lee, H. Fritze, and Y. Ogura, Progress in Ceramic Gas Turbine Development, Vol. 2. Edited by M. van Roode, M. Ferber, and D. W. Richerson, ASME PRESS, New York, NY, 641-664 (2003).
13. K. N. Lee, D. S. Fox, J. I. Eldridge, D. Zhu, R. C. Robinson, N. P. Bansal, and R. A. Miller, J. Am. Ceram. Soc. 86 [8] (2003): 1299-1306.
14. H. E. Eaton, G. D. Linsey, K. L. More, J. B. Kimmel, J. R. Price, and N. Miriyala, ASME paper 2000-GT-0631, International Gas Turbine and Aeroengine Congress and Exposition, Munich, Germany, May 8-11, 2000.
15. See note 7 above.
16. See note 3 above.
17. D. R. Clarke, Surface and Coatings Technology, 163-164, (2003): 67-74.
18. A.G. Evans, D. R. Mumm, J. W. Hutchinson, G. H. Meier and F. S. Pettit, Progress in Materials Science 46 (2001): 505-553.
19. M. K. Ferber, J. P. Singh, J. A. Haynes, M. Lance, I. G. Wright, H. Wang, and G. Romanoski, Advanced Turbine Systems Program 1998 Annual Report, Department of Energy (1998); B. A. Pint, I. G. Wright, W. Y. Lee, Y. Zhang, K. Pruβner, and K. B. Alexander, Mater. Sci. Eng., A145, 201-211 (1998); I. G. Wright and B. A. Pint, 1st Int. Conf. on Industrial Gas Turbine Technology (CAME-GT), Brussels, Belgium, July 10-11, 2003.
20. J. Cheng, E. H. Jordan, B. Barber, and M. Gell, Acta Mater., 46 [16] (1998): 5839-5850; also see note 18 above.
21. Y. Zhang, J. A. Haynes, B. A. Pint, I. G. Wright, and W. Y. Lee, Surface and Coatings Technology, 163-164, 19-24 (2003); M. W. Chen, R. T. Ott, T. C. Hufnagel, P. K. Wright, and K. J. Hemker, Surface and Coatings Technology, 163-164, 25-30 (2003);V. K. Tolpygo and D. R. Clarke, Acta Mater. 48, 3283-3293 (2000); S. Darzens, D. R. Munn, D. R. Clarke, and A. G. Evans, Met. and Mater. Trans. A, 34A, 511-522 (2003);D. R. Mumm, A. G. Evans, and I. T. Spitsberg, Acta. Mater. 49, 2329-2340 (2001);M. Gell, K. Vaidyanathan, B. Barber, J. Cheng, and E. Jordan, Met. and Mater. Trans. A, 30A, 427-435 (1999);Y. H. Sohn, J. H. Kim, E. H. Jordan, and M Gell, Surface and Coatings Technology, 146-147, 70-78 (2001).
22. A. G. Evans, G. B. Crumley, and R. E. Demaray, Oxid. Met., 20 [5] (1983): 193;G. C. Chang and W. Phucharoen, Surface and Coatings Technology 30 (1987): 13-28; A. M. Freborg, B. L. Ferguson, W. J. Brindley, and G. J. Petrus, Mat. Sci. and Eng., A245 (1998): 182-190;E. P. Busso, J. Lin, S. Sakura, and M. Nakayama, Acta. Mater 49 (2001): 1515-1528; E. P. Busso, J. Lin, and S. Sakura, Acta. Mater 49 (2001): 1529-1536; see also notes 18 and 20.
23. R. A. Miller, J. L. Smialek, and R. G. Garlick, *Advances in Ceramics, Vol. 3, Science and Technology of Zirconia*. Edited by A. H. Heuer and L. W. Hobbs, American Ceramic Society, Columbus, OH, 241-251 (1981).
24. D. Zhu and R. Miller, Journal of Thermal Spray Technology, 9[2] (2000): 175-180.
25. J. R. Gross, M. N. Rahaman, and R. E. Dutton, Ceram. Trans 154 (2003): 311-320.
26. See note 3.
27. See note 19.

28. See note 3.
29. Ibid.
30. See note 21 (Tolpygo) and (Gell).
31. See note 3.
32. Ibid.
33. Ibid.
34. A. Rabiei and A. G. Evans, Acta. Mater., 48, (2000): 3963-3976.
35. J. A. Haynes, M. J. Lance, B. A. Pint, and I. G. Wright, Surface and Coatings Technology 146-147 (2001): 140-146.
36. M. Gell, E. Jordan, and K. Vaidyanathan, Surface and Coatings Technology, 120-121, (1999): 53.
37. See note 19.
38. E. J. Felten, Oxid. Metals 10 (1976) 23-28; E. J. Felten and F. S. Pettit, Oxid. Metals, 10, 189-223 (1976); J. G. Fountain, F. A. Golightly, F. H. Stott, and G. C. Wood, Oxid. Metals 10 (1976): 341-345.
39. See note 19 (Wright & Pint).
40. See note 19 (Pint, et al.).
41. Ibid.
42. P. Y. Hou and J. Stringer, Oxid. Metals 38 (1992): 323-345; H. J. Grabke, G. Kurbatov, and H. J. Schmutzler, Oxid. Metals 43 (1995): 97-114.
43. See note 19 (Pint, et al.).
44. W. P. Allen and N. S. Bornstein, *High Temperature Coatings I*. Edited by N. Dahotre, J. M. Hampikian, and J. Stiglich, TMS, Warrendale, PA, 193-202 (1995); G. H. Meier, F. S. Pettit, and J. L. Smialek, Mater. Corros. 46 (1995): 232-240; M. A. Smith, W. E. Frazier and B. A. Pregger, Mater. Sci. Eng., A203, 388-398 (1995); J. C. Schaeffer, W. H. Murphy, and J. L. Smialek, Oxid. Metals 43 (1995): 1-23.
45. B. A. Pint, Oxid. Metals 45 (1996): 1-37.
46. Ibid.
47. See note 19 (Pint, et al.).
48. See note 19 (Pint, et al.) and (Wright & Pint).
49. See note 19 (Wright & Pint).
50. See note 19 (Pint, et al.).
51. Ibid.
52. See note 35.
53. See notes 3 and 19 (Wright & Pint).
54. See note 3.
55. See note 21 (Zhang, et al.), (Chen, et al.), and (Tolpygo & Clarke).
56. See notes 21 (Sohn, et al.) and 34.
57. See note 34.
58. See note 21 (Tolpygo & Clarke).
59. See note 21 (Zhang, et al.), (Chen, et al.), (Tolpygo & Clarke), and (Darzens, et al.).
60. Ibid.
61. See note 21(Chen et al.).
62. Ibid.
63. See note 21 (Zhang, et al.) and (Chen, et al.).
64. See note 21 (Zhang, et al.).
65. See note 21 (Zhang, et al.) and (Chen, et al.).
66. See note 21 (Tolpygo & Clarke).
67. See note 21 (Darzens et al.).
68. See note 21 (Mumm et al.).
69. See note 21 (Gell et al.).
70. D. R. Mumm and A. G. Evans, Acta Mater. 48, (2000): 1815.
71. See note 21 (Tolpygo & Clarke) and (Mumm et al.).
72. See note 21 (Mumm et al.).
73. See note 21 (Tolpygo & Clarke) and (Mumm et al.).
74. *Handbook of Thermal Spray Technology*. Edited by J. R. Davis, ASM International, Metals Park, OH, 2004.
75. A. H. Bartlett and R. Dal Maschino, J. Am. Ceram. Soc. 78 (1995): 1018.
76. J. R. Nicholls, K. J. Lawson, A. Johnstone, and D. S. Rickerby, Surface and Coatings Technology 151-152 (2002): 383-391.
77. D. S. Duvall and D. L. Ruckler, ASME Paper 82-GT-327 (1982).
78. U. Schulz, K. Fritscher, H.-J. Ratzer-Scheibe, et al., High Temperature Corrosion 4, Edited by R. Streiff, J. Stringer, R. Krutenat, M. Caillet, and R. Rapp, Trans Tech Publication, 957-964 (1997).
79. J. R. Nicholls, Y. Jaslier, and D. S. Rickerby, 4th Int. Symp. On High Temperature Corrosion, Les Embiez, France, May, 1996.
80. See note 78.

81. P. G. Klemens and M. Gell, Mater. Sci. Eng, A245 (1998): 143-149.
82. Ibid.
83. Ibid.
84. Ibid.
85. See notes 17 and 81.
86. See notes 76 and 81.
87. See note 81.
88. S. Raghavan, H. Wang, R. B. Dinwiddie, W. D. Porter, and M. J. Mayo, Scripta Materialia, 39[8] (1998): 1119-1125; J. –F. Bisson, D. Fournier, M. Poulain, O. Lavigne, and R. Mevrel, J. Am. Ceram. Soc. 83, (2000): 1993.
89. See note 17.
90. See note 81.
91. Ibid.
92. Ibid.
93. See note 17.
94. See notes 17 and 76.
95. See note 76.
96. Ibid.
97. D. S. Rickerby, European Patent EP 0 825 271 A1.
98. D. Zhu and R. A. Miller, Ceram. Eng. Sci. Proc. 23[4] (2002): 457-468.
99. Ibid.
100. J. R. Nicholls, K. J. Lawson, A. Johnston, and D. S. Rickerby, *High temperature corrosion 5*. Edited by R. Streiff, I. J. Wright, R. Krutenat, M. Caillet, and A. Cailerie, Trans Tech Publication, 595-606 (2001).
101. Ibid.
102. See note 76.
103. Ibid.
104. See note 24.
105. V. Lughi, V. K. Tolpygo, and D. R. Clarke, Mater. Sci. Eng. A368 (2004): 212-221.
106. Ibid.
107. See note 25.
108. See note 98.
109. See note 23.
110. Ibid.
111.Ibid..
112. Ibid.
113. S. Stecura, NASA TM 78976 (1978).
114. U. Schulz, , J. Am. Ceram. Soc. 83 (2000): 904-910.
115. H. G. Scott, J. Mater. Sci. 10 (1975): 1527-1535.
116. U. Schulz, K. Fritscher, and M. Peters, J. Eng. Gas Turbines Power 119 (1997): 817-21.
117. J. R. Van Valzah and H. E. Eaton, Surf. Coat. Technol. 46 (1991): 289-300.
118. See note 114.
119. D. J. M. Bevan and E. Summerville, *Handbook on the Physics and Chemistry of Rare Earths: Non-Metallic Compounds I.* Edited by K. A. Gschneider and L. R. Eyring, North-Holland Physics Publishing. New York, 412-515 (1979); M. A. Subramanian and A. W. Sleight, *Handbook on the Physics and Chemistry of Rare Earths: Non-Metallic Compounds I.* Edited by K. A. Gschneider and L. R. Eyring, Elsevier Science Publishers, Oxford, UK, 225-248 (1993).
120. Ibid.
121. M. J. Maloney, U.S. Patent No. 6 117 560, 2000; M. J. Maloney, U.S. Patent No. 6 284 323, 2001; G. Suresh, G. Seenivasan, M. V. Krishnaiah, and P. S. Murti. J. Nucl. Mater., 249, 259-61 (1997); G. Suresh, G. Seenivasan, M. V. Krishnaiah, and P. S. Murti. J. Alloys Compd., 269, L9-L12 (1998).
122. J. Wu, X. Wei, N. P. Padture, P. G. Klemens, M. Gell, E. Garcia, P. Miranzo, and M. I. Osendi, J. Am. Ceram. Soc. 85 (2002): 3031-3035.
123. Ibid.
124. Ibid.
125. R. Vassen, X. Cao, F. Tietz, D. Basu, and D. Stover, J. Am. Ceram. Soc. 83 (2000): 2023-2028.
126. Ibid.
127. R. Vassen, X. Cao, F. Tietz, and D. Stover, Ceram. Eng. Sci. Proc. 22 [4] (2001): 435-442.
128. Ibid.
129. R. A. Miller and G. W. Leissler, NASA TP 3296 (1993).
130. N. P. Padture and P. G. Klemens, J. Am. Ceram. Soc., 80, (1997): 1018-1020.
131. P. K. Wright, Mater. Sci. Eng. A245 (1998): 191; P. K. Wright and A. G. Evans, Curr. Opin. Solid State Mater. Sci. 4 (1999): 255.
132. See note 18.

133. See note 34.
134. S. R. Choi, J. W Hutchinson, and A. G. Evans, Mech. Mater. 31 (1999): 431; also see note 18.
135. See note 131 (Wright, 1998).
136. See note 34.
137. Ibid.
138. D. R. Mumm and A. G. Evans, Acta Mater 48 (2000): 1815-1827.
139. Ibid.
140. K. N. Lee, Surface and Coatings Technology, 133-134, 1-7 (2000); also see note 12.
141. K. N. Lee, D. S. Fox, and N. P. Bansal, J. Euro. Ceram. Soc. 25 (2005): 1705-1715.
142. N.S. Jacobson, D.S. Fox, J.L. Smialek, E.J. Opila C. Dellacorte, and K.N. Lee, ASM Handbook, Vol. 13B. Edited by S.D. Cramer and B.S. Covino, Jr., ASM International, Materials Park, OH, 565-578 (2005).
143. M. L. Auger and V. K. Sarin, Surface and Coatings Technology 94-95 (1997): 46-52 ; S. N. Basu, P. Hou, and V. K. Sarin, International Journal of Refractory Metals & Hard Materials 16 (1998): 343-52; J. A. Haynes, K. M. Cooly, D. P. Stinton, R. A. Lowden, and W. Y. Lee, Ceram. Eng. and Sci. Proceedings, 20 [4] (1999): 355-362 ; J. A. Haynes, M. J. Lance, K. M. Cooley, M. K. Ferber, R. A. Lowden, and D. P. Stinton, J. Am. Ceram. Soc. 83 [3] (2000): 657-659; Y. W. Bae, W. Y. Lee, and D. Stinton, J. Am. Ceram. Soc., 78 [5] (1995): 1297-300; W. Y. Lee, Y. W. Bae, and D. P. Stinton, J. Am. Ceram. Soc., 78 [7] (1995): 1927-30.
144. See note 12.
145. See note 13.
146. R. C. Robinson and J. L. Smialek, J. Am. Ceram. Soc. 82 [7] (1999): 1817-25 .
147. D. Zhu, K. N. Lee, and R. A. Miller, Ceram. Eng. Sci. Proc., 22 [4] (2001): 443-452.
148. See note 140.
149. J. I. Federer, J. Mater. Eng. 12 (1990): 141-149; D. W. Richerson and J. L. Schienle, Proceedings of the Twenty-Second Automotive Technology Development Contractors' Coordination Meeting (October 29-November 2, 1984), SAE P-155, 453-461, March 1985; J. R. Price, M. van Roode, and C. Stala, Key Engineering Materials 72-74 (1992): 71-84; K. N. Lee, R. A. Miller, and N. S. Jacobson, J. Am. Ceram. Soc. 78 [3] (1995): 705-710.
150. See note 140.
151. See note 149 (Lee et al.).
152. Ibid.
153. K. N. Lee, Transactions of the ASME 122 (2000): 632-636.
154. W. Y. Lee, K. L. More and Y. W. Bae, J. Am. Ceram. Soc. 79 [9] (1996): 2489-92.
155. See notes 13 and 140.
156. K. N. Lee, J. I. Eldridge, and R. C. Robinson, J. Am. Ceram. Soc., 88 [12] (2005): 3483-3488.
157. See note 153.
158. See note 156.
159. See notes 13 and 140.
160. See note 141.
161. H. E. Eaton, G. D. Linsey, E. Y. Sun, K. L. More, J. B. Kimmel, J. R. Price, and N. Miriyala, ASME paper 2001-GT-0513 ASME TURBOEXPO 2001, New Orleans, Louisiana, June 4-7, 2001; K. L. More, P. F. Tortorelli, L. R. Walker, J. B. Kimmel, N. Miriyala, J. R. Price, H. E. Eaton, E. Y. Sun, and G. D. Lindsey, ASME paper 2002-GT-30630, Proceedings of ASME Turbo Expo 2002, Amsterdam, Netherlands, June 3-6, 2002,
162. See note 13.
163. See note 161 (More et al.).
164. K.N. Lee, US patent 6,759,151 (2004); also see note 141.
165. See note 141.
166. P. Meschter, GE Global Research Center, private communication.
167. T. Ohji, The 28th Int. Conf. & Exp. On Adv. Ceram. & Composites, Cocoa Beach, FL (2004); H. Klemm, M. Fritsch, and B. Schenk, The 28th Int. Conf. & Exp. On Adv. Ceram. & Composites, Cocoa Beach, FL (2004); S. Ueno, D. D. Jayaseelan, N. Kondo, T. Ohji, and S. Kanzaki, The 28th Int. Conf. & Exp. On Adv. Ceram. & Composites, Cocoa Beach, FL (2004).
168. See notes 141 and 142.
169. K. N. Lee, unpublished research, NASA Glenn Research Center.
170. See notes 13 and 141.
171. See note 169.
172. See note 13.
173. See note 169.
174. C. M. Weyant, K. T. Faber, J. D. Almer, and J. V. Guibeen, J. Am. Ceram. Soc. 88 [8] (2005): 2169-76.
175. See note 141.
176. Ibid.
177. See note 144 (Lee et al.).
178. See note 167 (Ohji) and (Ueno, et al.).

BIOGRAPHY

4.4.2 Protective Coatings for Gas Turbines

Kang N Lee

Cleveland State University
NASA Glenn Research Center
Cleveland, OH 44135

Current Address:
Rolls-Royce Corporation
P.O. Box 420, Speed Code W-08
Indianapolis, IN 46206

phone: (317) 230-4469
email: kang.n.lee@rolls-royce.com

Kang Lee is a pioneer in environmental barrier coatings (EBC) for silicon-based ceramics. He played a key role in the development of the current state-of-the-art EBC. He has also investigated thermal barrier coatings (TBC) based on silicates and developed an emission spectroscopic non-destructive evaluation (NDE) technique for high temperature coatings. His current research focuses on development of advanced EBC for silicon carbide ceramic matrix composite (CMC) turbine hot section components and applying emission spectroscopic NDE to TBC. He has 13 U.S patents and has written two invited book chapters and over 50 technical publications.